Atmospheric Processes and Climatological Characteristics of the 79N Glacier (Northeast Greenland)

JENNY V. TURTON AND THOMAS MÖLG

Climate System Research Group, Institute of Geography, Friedrich-Alexander University, Erlangen-Nürnberg, Erlangen, Germany

DIRK VAN AS

Geological Survey of Denmark and Greenland, Copenhagen, Denmark

ABSTRACT

The Nioghalvfjerdsfjorden glacier (the 79 fjord, henceforth referred to as 79N) has been thinning and accelerating since the early 2000s, as a result of calving episodes at the front of the glacier. As 8% of the Greenland Ice Sheet area drains into 79N, changes in the stability of 79N could propagate into the interior of Greenland. Despite this concern, relatively little is known about the atmospheric conditions over 79N. We present the surface atmospheric processes and climatology of the 79N region from analyses of data from four automatic weather stations (AWS) and reanalysis data from ERA-Interim. Over the floating section of the glacier, the annual average air temperature is $-16.7°C$, decreasing to $-28.5°C$ during winter. Winds over the glacier are predominantly westerly and are of katabatic origin. Over the last 39 years the near-surface air temperature has increased at a rate of $+0.08°C\ yr^{-1}$. In addition, we find that large, rapid (48 h) temperature increases ($>10°C$) occur during the five-month dark period (November–March). Eight (±4) warm-air events occur annually from 1979 to 2017. We use the Weather Research and Forecasting (WRF) Model to simulate a particular warm-air event with above-freezing air temperatures between 30 November and 2 December 2014. The warm event was caused by warm-air advection from the southeast and a subsequent increase in the longwave radiation toward the surface due to low-level cloud formation. The frequent nature of the temperature jumps and the magnitude of the temperature increases are likely to have an impact on the surface mass balance of the glacier by bringing the skin temperatures to the melting point.

1. Introduction

Mass loss from the Greenland Ice Sheet (GIS) quadrupled between 1992 and 2011, largely because of a decreasing mass balance of -142 ± 49 gigatons (Gt) yr^{-1} and periods of accelerated ice velocity (the speed at which ice is transported from the interior to the coast) in the twenty-first century (Shepherd et al. 2012). The mass loss is mostly focused around the coast of Greenland, where numerous marine-terminating glaciers have retreated and thinned (Schaffer et al. 2017). One such glacier is the Nioghalvfjerdsfjorden glacier, Danish for 79 fjord glacier (hereafter 79N). 79N has a broad floating glacier tongue measuring approximately 80 km in the

west–east direction (Figs. 1c,d). The width of the glacier varies from approximately 21 km wide at its midpoint to 30 km wide at the calving front (Thomsen et al. 1997). Approximately 8% of the GIS area drains into 79N through the fast-flowing northeast ice stream (Huybrechts et al. 1999; Seroussi et al. 2011). Comparatively, a large outlet glacier in the west, Jakobshavn, drains approximately 6.5% of the GIS (Joughin et al. 2004).

The northeast ice stream extends 600 km into the interior of the GIS, and has the potential to increase sea levels by 1.1 m under the (albeit unlikely) case of complete collapse of this section (Mayer et al. 2018). Prior to the twenty-first century, the ice stream, and by association 79N, were believed to be stable, with only small elevation changes observed (Khan et al. 2014; Mayer et al. 2018). Since 2006 however, increasingly larger areas of the northeast ice stream ($840\ km^2$ in 2003 increasing to $7747\ km^2$ by 2009) have undergone pronounced thinning of $1\ m\ yr^{-1}$ (Khan et al. 2014).

ⓐ Denotes content that is immediately available upon publication as open access.

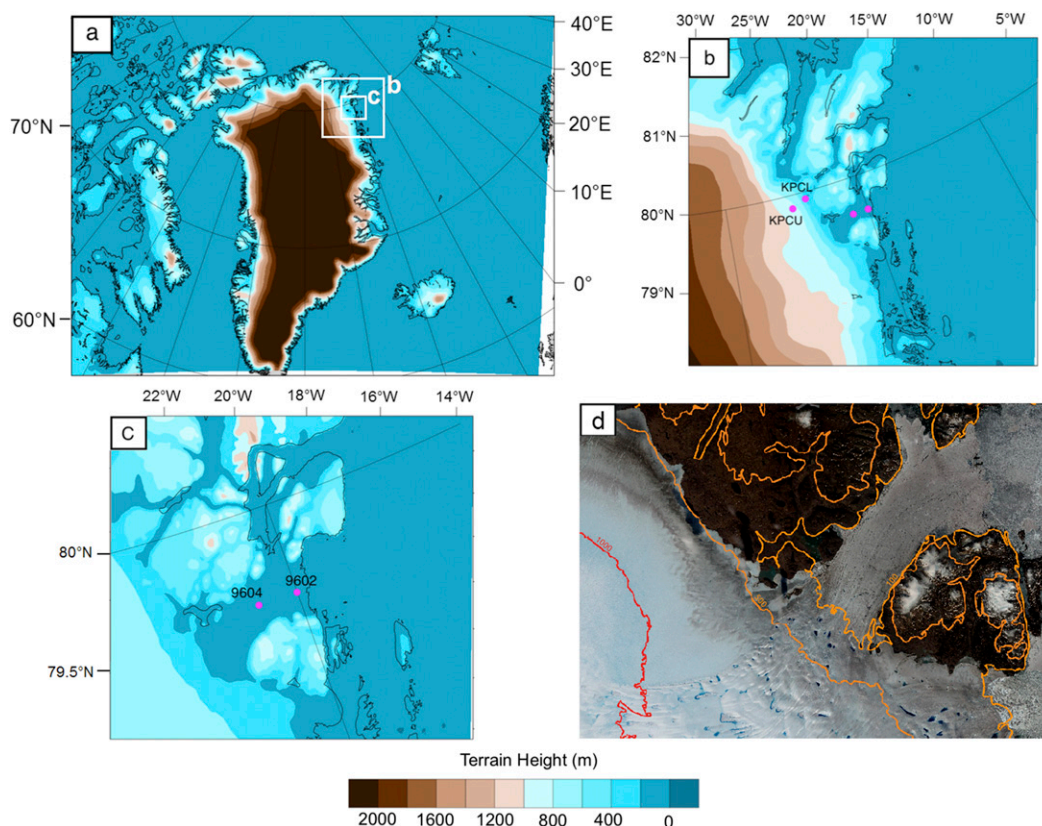*Corresponding author*: Jenny V. Turton, jenny.turton@fau.de

FIG. 1. (a) Location of the three domains used in the WRF case study. White boxes highlight the locations in (b) and (c). The four pink dots in (b) mark the location of the AWSs, with focus on KPC_U and KPC_L. (c) 9602 and 9604 AWSs are inside domain 3. Colored contours are terrain height (m). (d) Merged satellite images of 79N glacier from *Sentinel-2A* satellite, with elevation data from GIMP digital elevation model. The red contour is at 1000 m and the orange contours are 500 and 100 m.

Between 2009 and 2012, the floating ice shelf of 79N retreated by 2–3 km (Khan et al. 2014), and now features persistent surface meltwater drainage patterns including rivers and lakes (P. Hochreuther and A. Humbert, June 2018, personal communication). The main concern for the near future is that changes in dynamic stability of 79N (increased thinning and discharge of ice into the oceans) could propagate upstream and influence the mass balance of the vast interior of the ice sheet.

Reeh et al. (1999) stated that the mass balance of the 79N ice shelf was controlled by both subsurface and surface melting. More recently, Khan et al. (2014) concluded that a combination of increased regional air temperature, which led to reduced sea ice in front of the glacier, and the intrusion of warm subsurface water, triggered the mass loss and instability of 79N and nearby glaciers. It has also been shown that the northeast ice stream was sensitive to subtle changes in climate, and regularly underwent ice extent fluctuations and changes in margin (ice edge) location, in the

last 45 000 years (Larsen et al. 2018). Zachariae Isstrøm is a glacier immediately to the south of 79N (78.0°N), which currently loses 5 Gt yr^{-1} of ice (Mayer et al. 2018). It is likely that the higher calving rates and retreat of Zachariae are linked to the loss of sea ice and increased glacier melting from increased air temperatures (Mayer et al. 2018).

Despite the likely influence of regional air temperature changes on the surface of 79N and the immediate area, the majority of studies have focused on the influence of ocean circulation and bathymetry on the subsurface of the glacier (e.g., Mayer et al. 2000; Carr et al. 2013; Schaffer et al. 2017). Studies focusing on atmospheric temperature changes have assessed Greenland as a whole (Hall et al. 2008) or large sections of Greenland (Box et al. 2009), or they have focused on specific processes such as extreme warming during the summer (Leeson et al. 2018) or katabatic winds (Heinemann and Klein 2002). Furthermore, these studies often use a number of sporadic inland observation sites, the results of which cannot be extrapolated to a localized

TABLE 1. Information on the location, altitude, and observational period for the four AWS datasets used. T, air temperature; RH, relative humidity; WS, wind speed; WD, wind direction; P, air pressure; SW, shortwave radiation; LW, longwave radiation; CC, cloud cover; and TSK, skin temperature. A plus sign indicates that wind direction data were recorded by the logger, but the reference direction was not recorded. Therefore, wind direction data cannot be used with accuracy. An asterisk indicates that there is a gap between 15 Jan 2010 and 18 Jul 2012. KPC AWS data are available from 19 Jul 2008, but are only used beginning on 1 Jan 2009.

AWS Name	Lat (°N)	Lon (°E)	Elevation (m)	Start date	End date	Variables observed
9602	79.54	−20.01	43	3 Aug 1996	17 Aug 1997	T, RH, WS, WD$^+$
9604	79.54	−21.11	59	6 May 1997	30 July 1999	T, RH, WS, WD$^+$
KPC_U	79.83	−25.17	870	1 Jan 2009	1 Jan 2018	P, T, RH, WS, WD, SW$_{in}$, SW$_{out}$, LW$_{in}$, LW$_{out}$, CC, TSK
KPC_L	79.91	−24.08	370	1 Jan 2009	1 Jan 2018*	P, T, RH, WS, WD, SW$_{in}$, SW$_{out}$, LW$_{in}$, LW$_{out}$, CC, TSK

coastal region such as 79N. A recent study by Kuipers Munneke et al. (2018) highlighted the importance of understanding the year-round climatology and atmospheric processes in the polar regions, as intense winter melting episodes have been observed in the Antarctic Peninsula. A dedicated study for the atmospheric conditions over 79N glacier and the surrounding area is not yet available. To assess the present and future response of 79N in a warming world, it is important to gain insight into the surface mass changes of 79N, which are strongly coupled to the near-surface atmospheric conditions. This paper forms the basis of further research by detailing the local climate of the region and highlighting the atmospheric processes that may contribute to surface melting of the 79N glacier.

We use previously unpublished near-surface observations from the only meteorological field campaign known to have taken place on 79N from 1996 to 1999, and two on-ice automatic weather stations (AWSs) from nearby Crown Prince Christian Land (Kronprins Christian Land; Fig. 1), to investigate the meteorology and atmospheric processes present in this region. Because of the relatively short observational period in northeast Greenland (and especially over 79N glacier, where only four incomplete years of data are available), reanalysis data are used to extend the climatology back to 1979, within the region. A regional case study using the Weather Research and Forecasting (WRF) Model complements the observations and provides additional information on the links between synoptic-scale dynamics and the local climate. The data and methods used are outlined in the following section. In the results section (section 3), first reanalysis and observational datasets are compared to validate the ERA-Interim data used to investigate the climatology of the region (section 3a). Second, the observed atmospheric conditions and climatology of 79N are presented (section 3b). Sections 3c and 3d then follow, where we present the long-term climatic conditions over the glacier and the occurrence of warm-air events,

respectively. Finally, we present the case study of a warm-air event over 79N glacier (section 3e).

2. Data and methods

The only atmospheric field campaign to date on the floating ice shelf of 79N took place from August 1996 to August 1999 and was carried out by the Greenland Geologic Survey (GGU) at the Geological Survey of Denmark and Greenland (GEUS) (Thomsen et al. 1997). These data have not previously been analyzed in detail nor published. Four AWSs were erected on the floating ice shelf during these campaigns. However, only two stations have useable data because of data retrieval problems (Fig. 1c). AWS 9602, located at 79.54°N, 20.01°W, 43 m above sea level (MSL), was operational between 3 August 1996 and 17 August 1997. AWS 9604 (79.54°N, 21.11°W, 59 m MSL), was located at a 22-km distance away from 9602, and was operational from 6 May 1997 to 30 July 1999 (see Table 1 for data coverage). Because of complexities with logging data and upkeep of the stations, only near-surface air temperature, relative humidity, and wind speed data are found to be reliable and are used in this study at hourly intervals. Established post processing techniques (van den Broeke et al. 2004; Mölg et al. 2009) were used to remove erroneous data points due to riming, and wind direction data were removed because of large, consistent offsets when compared with other AWS and reanalysis data. Data during the winter period are missing for AWS 9604.

Observational data from the Programme for Monitoring of the Greenland Ice Sheet (PROMICE) network, operated by GEUS, are also used to gain a broader understanding of the local climate. Data from two AWSs located on Kronprins Christian Land (KPC), which is located to the northwest of 79N, have been analyzed here. AWS KPC_U is located at 79.83°N, 25.17°W, 870 m MSL, and KPC_L is located at 79.91°N, 24.08°W, 370 m MSL (Fig. 1b). Both AWS were erected

TABLE 2. Comparison of both ERA-I and MERRA2 reanalysis products with 6-hourly instantaneous observations from three AWS sites (AWS 9604 is not included because of the intermittent and short observational period). See Table 1 for data availability. Biases are calculated as differences between reanalysis and AWS over the same period as observations. RH and WS are analyzed as annual averages, whereas temperature is averaged annually and during the winter. DJF corresponds to winter values. An asterisk indicates that differences between the reanalysis product and AWS are statistically significant at 95% confidence level, while a double asterisk is significance at 99% level, using an ANOVA test for biases.

Location variable	AWS average	ERA-I mean bias	MERRA2 mean bias	ERA-1 correlation	MERRA2 correlation	ERA-1 RMSE	MERRA2 RMSE
9602 annual T (°C)	−16.4	0.8	3.4**	0.95	0.88	4.9	7.7
KPC_U annual T (°C)	−16.6	1.4**	0.1	0.97	0.9	3.3	2.4
KPC_L annual T (°C)	−13.4	−2.2**	−3.8*	0.97	0.89	3.5	4.4
9602 DJF T (°C)	−32.6	3.1	10.7**	0.9	0.3	6.5	12.4
KPC_U DJF T (°C)	−27.4	0.8**	1.9**	0.86	0.45	3.4	5.7
KPC_L DJF T (°C)	−23.9	−3.1**	4.3**	0.84	0.4	4.6	6.3
9602 RH (%)	87.0	9.5**	−5.5**	0.6	0.2	12.3	12.2
KPC_U RH (%)	83.6	−6.2**	3.9**	0.39	0.26	3.1	10.6
KPC_L RH (%)	73.6	3.6*	−3.7**	0.44	0.4	10.1	10.7
9602 WS (m s^{-1})	2.4	0.4*	1.2**	0.52	0.2	2.3	5.1
KPC_U WS (m s^{-1})	4.9	0.2**	−0.7	0.74	0.42	1.8	2.7
KPC_L WS (m s^{-1})	6.1	−1.5**	−1.9	0.7	0.56	2.9	2.9

on 19 July 2008 and remain operational to this day. Because of power-related issues, KPC_L data are missing between January 2010 and July 2012. The observed variables and locations of the weather stations are outlined in Table 1, and mapped in Fig. 1, respectively. See PROMICE documentation for information on processing and quality control of the data (www.promice.org/ PromiceDataPortal, last accessed on 20 March 2019).

Because of the relatively short and intermittent observing period of the AWSs, two reanalysis products are used to assess the climatology of the lower boundary layer over the glacier surface. The two products are the European Centre for Medium-Range Weather Forecasts (ECMWF) ERA-Interim dataset from 1979 to 2017, henceforth referred to as ERA-I, and the Modern-Era Retrospective Analysis for Research and Applications, version 2 (MERRA2), from 1980 to 2017. For information on the data assimilation and modeling involved in ERA-I and MERRA2, see Dee et al. (2011) and Gelaro et al. (2017), respectively. We evaluate climate conditions over 79N with both ERA-I and MERRA2 data based on findings by Reeves-Eyre and Zeng (2017) for the whole of Greenland. They concluded that MERRA2 performed well (mean absolute error <2°C) at reproducing the near-surface air temperature observations at 50 AWSs over the GIS, and ERA-I performed best at representing the 11 coastal station conditions, including the two KPC AWSs used in the current study (Reeves-Eyre and Zeng 2017). To have confidence in the climatology constructed using ERA-I and MERRA2 data, the reanalysis data are compared with AWS observations. Observed six-hourly instantaneous (0000, 0600, 1200, and 1800 UTC)

values from the AWSs have been compared with six-hourly instantaneous reanalysis products. Meteorological values of air temperature, relative humidity, wind speed, and direction from 79N are extracted from ERA-I or MERRA2 data at the closest grid point to the coordinates of the AWSs.

3. Results

a. Reanalysis–observations comparison

To gain information on the longer-term conditions and climatology of the lower atmospheric boundary layer over 79N, we must ensure that the reanalysis data are representative of the real conditions. Here, we compare the reanalysis products with 79N AWS data (Table 2). ERA-I and MERRA2 have relatively small mean biases for annual average temperature (e.g., 0.8°C bias for air temperature at AWS 9602 and ERA-I) and wind speed (0.2 m s^{-1} bias for wind speed at KPC_U and ERA-I); however, many of the differences are statistically significant at the 95% confidence level. Figure 2 shows that MERRA2 has difficulty representing the lower temperatures at AWS 9602, resulting in larger and significantly different mean biases (10.7°C) and root-mean-square error (RMSE) (12.4°C) than in ERA-I during winter (Table 2). ERA-I has higher positive correlations than MERRA2 for relative humidity, wind speed, and air temperature at all observational sites. MERRA2 has smaller mean biases than those of ERA-I for relative humidity observations at AWSs 9602 and KPC_U, but a larger magnitude bias for AWS KPC_L. However, all mean biases for relative humidity are statistically significant
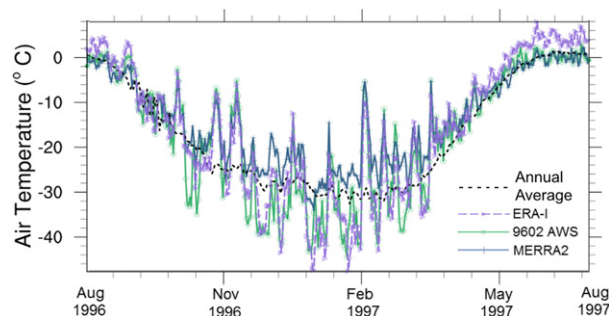
FIG. 2. Six-hourly air temperature observations from AWS 9602 (green line and circles), ERA-I (purple dashes and triangles), and MERRA2 (blue line and crosses) from 3 Aug 1996 to 2 Aug 1997. Warm-air events punctuate the seasonal temperature cycle. The black dashed line represents the 1979–2017 seasonal cycle from 3 Aug to 2 Aug calculated from ERA-I by averaging all temperature values for each six-hour period on each date from 1979 to 2017.

TABLE 3. Annual, summer (JJA), and winter (DJF) average observational values from AWS 9602, AWS KPC_U, and AWS KPC_L. AWS 9604 is not included because of the intermittent and short observational period. CC refers to cloud cover, and P is the air pressure at the station.

AWS and variable	Annual	JJA	DJF
9602 T (°C)	−16.4	−0.1	−32.6
KPC_U T (°C)	−16.6	−1.2	−27.4
KPC_L T (°C)	−13.4	1.8	−23.9
9602 RH (%)	87.0	89.2	88.5
KPC_U RH (%)	83.6	79.8	87.3
KPC_L RH (%)	73.6	71.9	76.3
9602 WS (m s^{-1})	2.4	2.0	1.9
KPC_U WS (m s^{-1})	4.9	4.3	4.7
KPC_L WS (m s^{-1})	6.1	3.9	5.9
KPC_U WD (°)	288	275	284
KPC_L WD (°)	308	308	326
KPC_U P (hPa)	905.9	911.1	901.0
KPC_L P (hPa)	966.0	967.2	962.2
KPC_U CC (fraction)	0.5	0.4	0.7
KPC_L CC (fraction)	0.5	0.4	0.6
KPC_U TSK (°C)	−17.8	−2.3	−29.0
KPC_L TSK (°C)	−14.6	−0.8	−25.9

at the 95th confidence level and most for the 99th confidence level. The mean biases for wind speed are consistently smaller in ERA-I than MERRA2. The RMSEs of MERRA2 are larger than those of ERA-I at the KPC stations, except for the annual temperature at KPC_U. In conclusion, ERA-I is generally able to more accurately represent the annual and winter temperature cycle at 79N on the floating tongue of the glacier (9602 and 9604) and farther inland (KPC_U and KPC_L) compared to MERRA2. Therefore, we use ERA-I to analyze the long-term characteristics, trends, and variability of atmospheric conditions from 1979 to 2017.

b. Observed atmospheric conditions of 79N

The observed annual average air temperature, relative humidity, and wind speed at AWS 9602 (August 1996–August 1997) were −16.4°C, 87.0%, and 2.4 m s^{-1}, respectively (Table 3). Because of the intermittent observations at AWS 9604, an observed annual average is not possible. The observed summer (JJA) average air temperature, relative humidity, and wind speed at AWS 9602 for 1997 were −0.1°C, 89.2%, and 2.0 m s^{-1}, respectively (Table 3). The observed AWS 9604 near-surface summer averages (1998 and 1999) were 0.7°C, 87.2%, and 1.5 m s^{-1}.

At KPC_L, on the sloping ablation area (the low-altitude zone with average mass loss due to melting and sublimation), the observed annual average values (2009–17) are −13.4°C (standard deviation, SD = 1.5°C), 73.6% (SD = 3.9%), 6.1 m s^{-1} (SD = 0.8 m s^{-1}), and 308° (SD = 15.3°) for air temperature, relative humidity, wind speed, and direction, respectively (Table 3). The coldest (annual average) location (−16.6°C, SD = 0.5°C)

in this study is found at the equilibrium line altitude (KPC_U AWS); the elevation at which mass gains by snowfall are offset by mass loss from melting and sublimation, separating the accumulation zone in the upper reaches of the glacier from the ablation zone below. Observed average annual relative humidity at KPC_U is 83.6% (SD = 4.5%) and wind speed and direction are 4.9 m s^{-1} (SD = 0.2 m s^{-1}) and 288° (SD = 4°), respectively (Table 3). The amplitude of the air-temperature cycle generally increases with latitude over Greenland: KPC_U AWS has the largest amplitude of all PROMICE AWSs on the GIS margin (van As and Fausto 2011). The summer conditions at KPC_U AWS are also cooler than over the floating glacier, with average summer air temperatures of −1.2°C (SD = 3.4°C). The summer average relative humidity, wind speed and wind direction for KPC_U are 79.8% (SD = 7.8%), 4.3 m s^{-1} (SD = 1.9 m s^{-1}), and 275° (SD = 43°), respectively (Table 3). On the sloping surface (KPC observations), winds are of katabatic origin; cold, downslope winds, as shown by the downslope wind direction and higher wind speeds observed at the slope stations compared to those on the floating glacier. Katabatic winds can be funneled by the complex topography, and intensify when forced through gaps such as those to the north of the main glacier valley (see Fig. 1c). Katabatic winds are especially prevalent during winter and are observed in many coastal areas of Greenland (van As et al. 2014).

The intraseasonal variability of a number of atmospheric variables is largest in winter (DJF) months, especially the near-surface air temperature (Figs. 2 and 3).
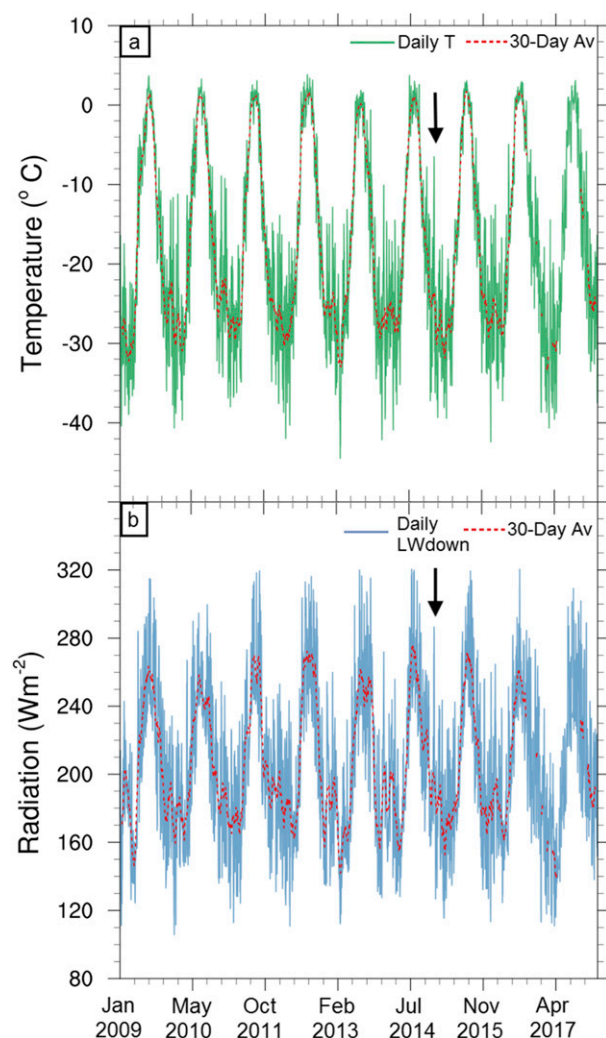
FIG. 3. (a) Daily air temperature (green) and (b) daily down-welling longwave radiation (blue) observed at KPC_U from 2009 to 2017 and 30-day moving averages (dashed red). The black arrows mark the warmest November-March daily average value for the 8-yr period (2 Dec 2014), and marks a day within the case study event presented in this paper.

At KPC_U AWS, the winter average temperature is −27.4°C, with an SD of 6.5°C; 3.1°C larger than during summer. In particular winters, the variability can be even larger, with winter 2013 experiencing an average winter temperature of −28.1°C and an SD of 7.5°C. Similarly, the variability in wind speed, wind direction and relative humidity is larger in winter than in summer. Cloud cover (fraction from 0 to 1) is estimated from downwelling longwave radiation and air temperature measured at the KPC weather stations (van As 2011). During summer at KPC_U, 26% of days have a cloud-cover fraction of less than 0.1 (clear skies), while during winter, this number decreases to 6% of days. Similarly, during winter, 32% (219 days) of days

observed a cloud-cover fraction of greater than 0.9 (full cloud cover), whereas in summer, only 6% of days experience overcast conditions. Over the Arctic Ocean, two well-defined wintertime cloud states have been identified from observations; radiatively clear and opaquely cloudy (Graham et al. 2017). Opaquely cloudy conditions occur under thick, mixed-phase clouds, associated with warm and moist air advected from midlatitudes, whereas radiatively clear conditions are associated with cloud-free conditions (Graham et al. 2017). A consequence of the opaquely cloud conditions is an increase in downward longwave radiation, which results in higher near-surface temperatures, similar to conditions observed at the KPC AWSs during the winter months (Figs. 3a,b).

c. Long-term climatic characteristics

The length of data availability from ERA-I allows us to examine the climatology of the 79N region, despite the short length of the AWS records on the floating glacier. Data from ERA-I are taken at the grid point located closest to the coordinates of AWS 9604 because of its central location on the floating glacier. The annual, JJA, and DJF average 2-m air temperatures from 1979 to 2017 are −16.7°, −0.4°, and −28.5°C, respectively. The average annual cycle in air temperature is presented on Fig. 2 (black line). The wind direction in all seasons is predominantly westerly (287°) because of the persistence of katabatic winds draining off the ice sheet.

From 1979 to 2017, the annual average air temperature trend is +0.08°C yr⁻¹ (3.0°C increase, significant at the 95% confidence level when performing an F test for trend significance) (Fig. 4). The number of months with an average temperature greater than 0°C has increased from 1.1 (SD = 0.4) per year for 1979–91 to 1.8 (SD = 0.8) per year for 2005–17. Similarly, the monthly average minimum and maximum temperatures have increased. The largest rate of change is seen during autumn (SON), during which average air temperature has increased by 0.12°C yr⁻¹ (±0.02°C, significant at 95% confidence level from an F test for trend significance). Box et al. (2009) found similar results when analyzing air temperature variability over Greenland from 1840 to 2007. Between 1994 and 2007, a warm period over Greenland was observed, which was attributed to large, positive autumn temperature anomalies and a warming trend that surpassed that of other seasons (Box et al. 2009). Figure 4 also highlights the cooler years, some of which are associated with volcanic eruptions. Most notable is the annual average temperature of −20.8°C following the eruption of El Chichón in 1982. Similar results were found by van As et al. (2018) when analyzing the summer air temperatures in the southwest of Greenland.
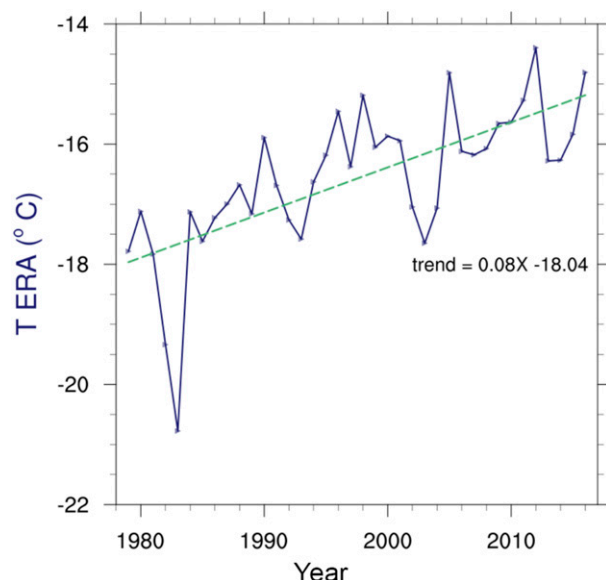
FIG. 4. The annual average air temperature from ERA-I at 79N (blue) and linear regression line (green dashed).

The rate of increase in air temperature observed over 79N ($+0.08°\text{C yr}^{-1}$) is slightly lower than observed over the west coast of Greenland ($+0.15°\text{C yr}^{-1}$) by Abermann et al. (2017). However, it is a similar magnitude to the warming trend found by Orsi et al. (2017) in the north of Greenland, during the North Greenland Eemian Ice Drilling project ($+2.7°\text{C}$ in 30 years). Mernild et al. (2014) identified a slower increasing trend of $+0.45°\text{C decade}^{-1}$ when averaging six coastal stations in east Greenland, compared to the trend observed solely over 79N. Therefore, although regionally the magnitude of the air temperature trend varies, an increase in air temperatures is not in debate. Over the same 37-yr period, there has been no significant change in the wind speed, and the wind direction has remained predominantly westerly. The mean sea level pressure (MSLP) has also remained approximately constant, with an average value of 1013.7 hPa month^{-1} from 1979 to 2017, and a nonzero decreasing trend of -0.1 hPa decade^{-1}. Abermann et al. (2017) identified larger negative trends in MSLP over the west and east coasts of Greenland when using a more widespread AWS network.

d. Warm-air events

Upon analysis of both the near-surface observations and the ERA-I data, we find particularly interesting departures from the sinusoidal temperature cycle during winter (Figs. 2 and 3), and much larger variability between 1 November and 31 March than observed in other months. To assess the frequency and characteristics

of these "warm-air events," we developed a method to distinguish the events from the temperature record. A probability density function of the change in the daily average temperature over a 48-h period was constructed using ERA-I data during 1 November to 31 March from 1979 to 2017. The warm-air events were identified as periods during which the change in the daily average temperature over a 48-h period was greater than the 95th percentile of all 48-h temperature changes. This 95th percentile threshold corresponds to a temperature change of 10.2°C or greater. The extended winter period was analyzed, as this is when large, sudden temperature changes are observed. However, when altering the months selected (e.g., 1 October to 1 March), the 95th percentile value changed only marginally, as the warm-air events are most frequent, and of the largest magnitude, between 1 November and 31 March.

Evidently, with every increase in temperature is a decrease of a similar magnitude after the event. We focus on only the positive temperature change because of the potential for these events to contribute to a change in the surface energy balance, specifically, via surface melting of the glacier. A recent study (Kuipers Munneke et al. 2018) highlighted the importance of investigating wintertime atmospheric processes in the polar regions. Wintertime melting episodes, driven by foehn winds (warm and dry downslope winds) over Larsen C ice shelf, prompted an earlier start of the melt season and allowed meltwater to penetrate into the ice shelf (Kuipers Munneke et al. 2018). In that location over Antarctica, melting was observed for three winters between 2015 and 2017, with the majority of melting observed during May 2016 (austral winter). In total, 23% of the annual melt amount occurred during winter (240-mm water equivalent) (Kuipers Munneke et al. 2018). While the processes responsible for wintertime melting over Larsen C identified by Kuipers Munneke et al. (2018) are not the same as the warm-air events observed over 79N, it is clear that the relationship between atmospheric processes and surface melting must not be dismissed, even during winter.

The warm-air events are evident in observations and in ERA-I in almost every extended winter period (November–March) from 1979 to 2017 over the glacier, with the exception of 1981 (when temperature increases were observed, but were not large enough to meet our threshold outlined above). The warm-air events are observed at all locations in our study period, even to an altitude of 870 m (KPC_U). Therefore, they are likely to be associated with synoptic processes, as the features are regional, as opposed to very localized.

At AWS 9602, there were 12 warm-air events with a temperature increase of $\geq$10.2°C in the one year of data.

During these events, the wind speed increases considerably by 4 to $10\,\mathrm{m\,s}^{-1}$. Both the temperature and wind speed are above average for the time of year and return to normal values within 2–4 days (Fig. 2). There is no associated decrease in relative humidity during these events, which suggests that foehn winds (downslope winds associated with significantly dry air) are not the primary mechanism responsible for the changes, although they are observed in many coastal regions of Greenland, including the northeast (R. Mottram, 2018, personal communication).

In KPC_U and KPC_L observations, the warm-air events are a persistent winter feature from 2009 to 2017 where large (≥ 10.2°C) and rapid (within 48 h) increases in temperature occur between 1 November and 31 March (Fig. 3a). The median number of warm-air events at KPC_U is 10 (SD = 4.0) events per year. At KPC_L, there are 11 events per year (SD = 4.6). The warm-air events are also evident in near-surface ERA-I data over the floating glacier. By analyzing only the periods with a temperature change of greater than 10.2°C (within 48 h), there are on average 8 (SD = 4) warm-air events each year between November and March. The highest number of events during one year was in 1 November 1997 to 31 March 1998, when 16 warm-air events occurred.

To assess the changes in temperature and MSLP associated with the warm-air events over the whole northeast Greenland region, composite plots of the warm-air events have been included. Similarly, composite differences between the warm-air events and the climatological means are presented (Figs. 5 and 6). To test for significance in the differences, the false discovery rate (FDR) field-significance test by Wilks (2016) has been used. This test reduces the number of false-positive significance results without applying a more conservative p value, and takes spatial autocorrelation into account (Wilks 2016). Our control-level p value is 0.01, which means that only grid cells with p values much less than our control will be significantly different in a spatial context (dots on the difference figures). Figure 5b presents the composite 2-m temperature field 48-h prior to all warm-air events between 1979 and 2017 within ERA-I. The air temperature change over the whole northeast region is statistically significantly warmer (+10°C) during warm-air events than the November–March average (Fig. 5f), which highlights the regional impact of the warm-air events. Conversely, 48-h prior to the warm-air events, slightly cooler-than-average air (−2°C but not significantly different) lies over the northeast of Greenland (Fig. 5c). Over the central and southeastern part of Greenland, the air is warmer than average prior to warm-air events,

although only a small region near the east coast is statistically significantly different.

The individual temperature increases are relatively short-lived; however, the +10°C increase due to synoptic influences is approximately a third of the +30°C temperature rise that occurs annually between the winter and summer because of solar radiation changes (observations from AWS 9602). The warm-air events, while having little impact on the average annual temperature value, do have an impact on the sinusoidal seasonal temperature cycle. As a consequence of these synoptic winter temperature increases, the air temperature during winter does not display a clear seasonal temperature cycle (Fig. 3a). Instead of continually decreasing temperatures into the winter due to the absence of solar radiation, between late November and early April, the monthly average air temperature stabilizes, leaving winter temperatures higher than expected for this latitude. A similar signal is also found in the skin temperature and incoming longwave radiation, whereby the mean values flatten out during winter, as measured at the KPC AWSs (Fig. 3b). "Coreless winters" typically occur in the polar regions when the seasonal temperature cycle does not display a typical sinusoidal curve because of a warmer-than-average (at this latitude) winter (Wexler 1958; Bednorz and Fortuniak 2011). This characteristic was first identified in the Antarctic by Wexler in 1958 and has since been observed in a number of polar locations (Bednorz and Fortuniak 2011; van As and Fausto 2011; Suparta et al. 2012). The 30-day moving average air temperature in Fig. 3a highlights the characteristics of coreless winters. Coreless winters, while evident in a number of locations, develop because of different synoptic processes, specific to each region.

We hypothesize that two mechanisms are responsible for the warm-air events within the 79N region: warm-air advection and mixing from katabatic winds. During winter, as the solar radiation decreases to $0\,\mathrm{W\,m}^{-2}$, the surface energy balance (SEB) and temperatures (air and surface) decrease and the lower atmospheric boundary layer begins to deepen. Coincidentally, cyclonic activity over the North Atlantic starts to increase. During winter, low pressure systems often develop and travel between Iceland and the east coast of Greenland, leaving a fingerprint in the climate signal (Fig. 6a). Under low pressure conditions to the southeast of Greenland, warm, moist air is advected toward 79N from over the Atlantic. Concurrently, the warmer and moister air creates a low-level cloud or fog level, which additionally warms the surface and air because of an increased downward flux of longwave radiation to the surface (Bednorz and Fortuniak 2012). We hypothesize
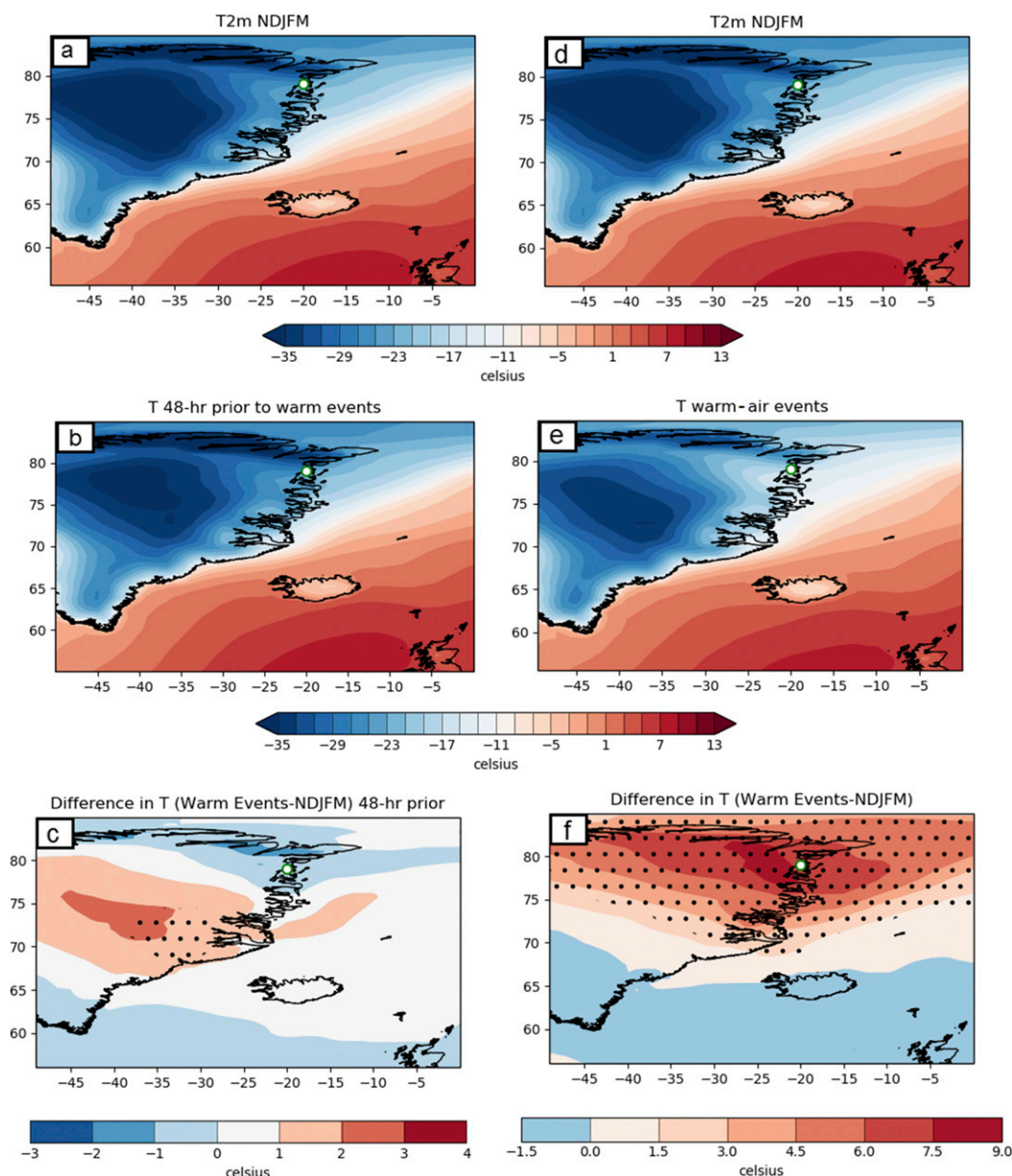
FIG. 5. (a),(d) Composite plots of 2-m air temperature for the 1979–2017 (ERA-I) extended winter period (November-March), (b) 48 h prior to warm-air events, and (e) during warm-air events. (c) The difference between (b) and (a) (48 h before − extended winter). (d) The difference between (e) and (d) (warm-air events − extended winter). The white circle highlights the location of 79N. NDJFM refers to the months November to March. In total, 295 warm-air events were used for the composite. Note the different scales used for (c) and (f). The dots infer that differences are statistically significant when using a p value of 0.01 for the FDR test by Wilks (2016).

that a combination of warm-air advection from the low pressure systems and low-level cloud formation are responsible for a number of the warm-air events. Tjernström et al. (2015) presented a case study of a warm-air advection episode that generated a temperature inversion and increased flux in the downwelling longwave radiation because of low-level clouds and fog over the Arctic sea ice. The impact of the winter cyclonic events on temperatures are well documented over Svalbard, where warming of +30°C can be observed during individual warm-air events (Graham et al. 2017; Rinke et al. 2017).

In other studies, katabatic winds have been responsible for increased near-surface air temperatures, as they
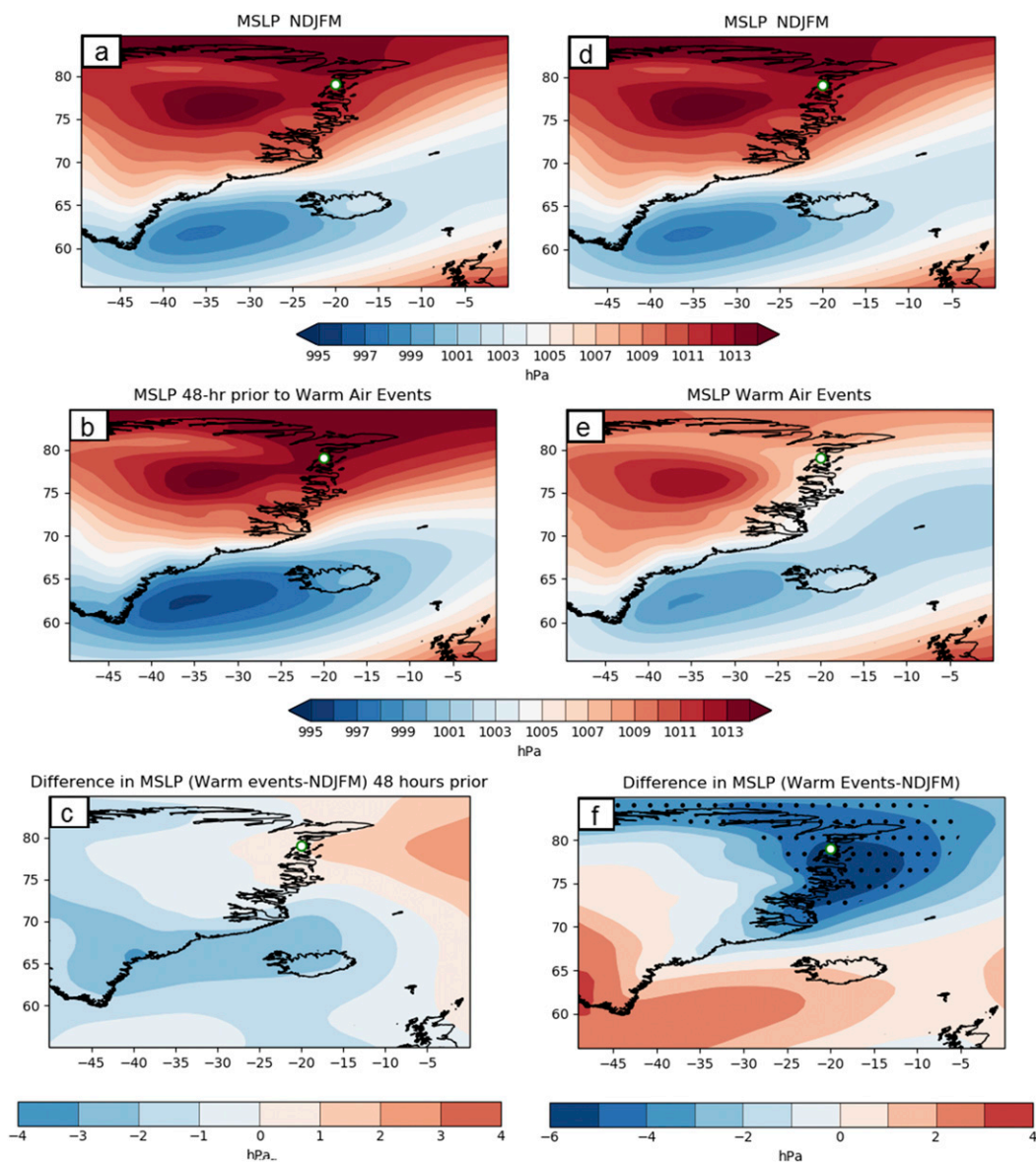
FIG. 6. As in Fig. 5, but with composite plots of MSLP rather than air temperature. Note the different scales used for (c) and (f). The dots infer that differences are statistically significant when using a p value of 0.01 for the FDR test by Wilks (2016).

mix potentially warmer air from aloft, down toward the surface under stable conditions (Vihma et al. 2011). As katabatic winds are the dominant wind processes over the sloped areas of 79N, this mechanism cannot be ruled out, and thus it is the hypothesized second mechanism responsible for warm-air events. We do not aim to quantify the mechanisms responsible in this study, but rather we aim to highlight which mechanisms are at play in this region. As two mechanisms are hypothesized we will present the characteristics of the warm-air events in general and distinguish them by wind direction in an attempt to separate the two mechanisms.

The floating section of the glacier is oriented toward the northeast (approximately 45°) and there are a number of small valleys and troughs to the north of the glacier (Fig. 1c). Therefore, drainage off the GIS and katabatic winds not only flow from the southwest down the main valley of the glacier but also span approximately 180° to 330°. Despite the wide angle, the direction of katabatic winds and the winds advected from the Atlantic (easterly sector) are never from the same direction, theoretically, making it relatively easy to separate the two processes. However, because of the lack of wind direction measurements at the AWSs on

the floating ice shelf, and the higher altitude of the KPC AWSs, this is not easy in reality.

As a way of differentiating between possible different mechanisms, the warm-air events have been binned into easterly and westerly events based on the daily wind direction. In approximately 30% of the warm-air events, the winds at the surface of the floating glacier (from ERA-I) are from an easterly sector (1°–179°). Under these conditions, warm and moist air is advected onto the glacier from the Atlantic, and the mechanism responsible for the warm-air events is most likely warm-air advection. The temperature advection close to the surface (between 1000 and 900 hPa) over 79N during all easterly warm-air events is $0.5 \, \mathrm{K \, h^{-1}}$. During individual events, the value increases to $1.3 \, \mathrm{K \, h^{-1}}$, providing evidence for advection of warm air from the Atlantic. These values are the same order of magnitude as during a warm-air advection case study observed in the east Siberian section of the Arctic circle (0.0–$0.8 \, \mathrm{K \, h^{-1}}$) (Sotiropoulou et al. 2018). In 25% of cases the wind direction was from an approximately up-valley, southwesterly direction (180°–270°) and is likely due to katabatic mixing. For the remaining warm-air periods, winds are from a westerly to northwesterly direction and are also likely associated with katabatic winds.

Figure 6e displays the MSLP from a composite of all warm-air events identified in ERA-I data from 1979 to 2017, and the average November–March MSLP during these years (Figs. 6a,d). Similarly, Fig. 6b presents the MSLP composite of 48-h prior to all warm-air events, in an effort to display the temporal evolution in the warm-air events. Prior to the warm-air events, the MSLP is deeper to the southeast of Greenland (−4 hPa, see Fig. 6c) than the extended winter climatological mean (however, none of the differences in this region were statistically significant). We hypothesize that this is due to the development of low pressure systems between Greenland and Iceland. Coinciding with this developing low pressure system, the air temperature 48 h prior to the warm-air events is warmer over the central part of Greenland, where warm-air is being advected from the Atlantic (Fig. 5c).

During the warm-air events, the low pressure system moves north and east along the east coast of Greenland, as shown by the elongated area of comparatively lower MSLP (Fig. 6e). Figure 6f shows that the MSLP is statistically significantly lower over the northeast of Greenland (negative differences of −6 hPa), and slightly higher (1.5–3.0 hPa) over the southeast of Greenland, than during average conditions between November and March. This bimodal response in the MSLP suggests that low pressure systems may pass closer and more frequently toward the northeast of Greenland, and that

cyclonic activity in the southeast of Greenland is less frequent, or in a different location, during warm-air events. Assessing the MSLP alone cannot distinguish whether warm-air advection or mixing from katabatic winds are responsible for the temperature increases. Similarly, assessing the MSLP of all warm-air events together may be masking the differences between events that are characterized by different prevailing wind directions. Therefore, Fig. 7 presents the MSLP during warm-air events separated by wind direction.

The largest temperature increases were associated with the easterly warm-air advection cases. Warm-air events with an easterly wind direction experienced an average temperature increase of 13.5°C, whereas those associated with westerly flow (we assume katabatic mixing) observed an average temperature increase of 12.5°C. This is significant at the 95% level when testing for significance using t test with unequal variances. Similarly, at KPC_U and KPC_L, the largest temperature increases were under easterly wind conditions. Figures 7c and 7f show the statistically significantly higher temperatures over northeast Greenland and lower MSLP (between Greenland and Iceland) associated with easterly wind (warm-air advection) events from ERA-I data from 1979 to 2017. The MSLP under westerly events is higher over the continent (Fig. 7d), which leads to clear skies that allow for cooling of the surface through a negative radiation budget, generating persistent katabatic winds (Vihma et al. 2011). Under these conditions, cold and dense air from the continent flows down steep topography to lower-elevation areas such as the floating tongue of 79N glacier. The turbulent nature of the winds interacting with statically stable air lying over the tongue leads to mixing of potentially warmer air from aloft toward the surface, and adiabatic heating of the air as the air mass descends down slopes (Vihma et al. 2011).

Cloud-cover observations at KPC_U and KPC_L reveal that under warm-air events with easterly winds, the average cloud-cover fraction is 0.81, whereas under katabatic or westerly wind conditions, the average cloud-cover fraction is 0.55. The November–March average cloud cover is 0.55 at KPC_U. Therefore, easterly wind events have above average cloud cover, which provides evidence for low-level cloud formation associated with easterly warm-air advection events over 79N. This was also observed during warm-air advection events over the Arctic Circle by Tjernström et al. (2015) and Tjernström et al. (2019). In particular, winter cyclones and their associated warm-air advection were responsible for wintertime sea ice melting and reduced sea ice growth to the north of Svalbard (Rinke et al. 2017). Previously, warm-air advection
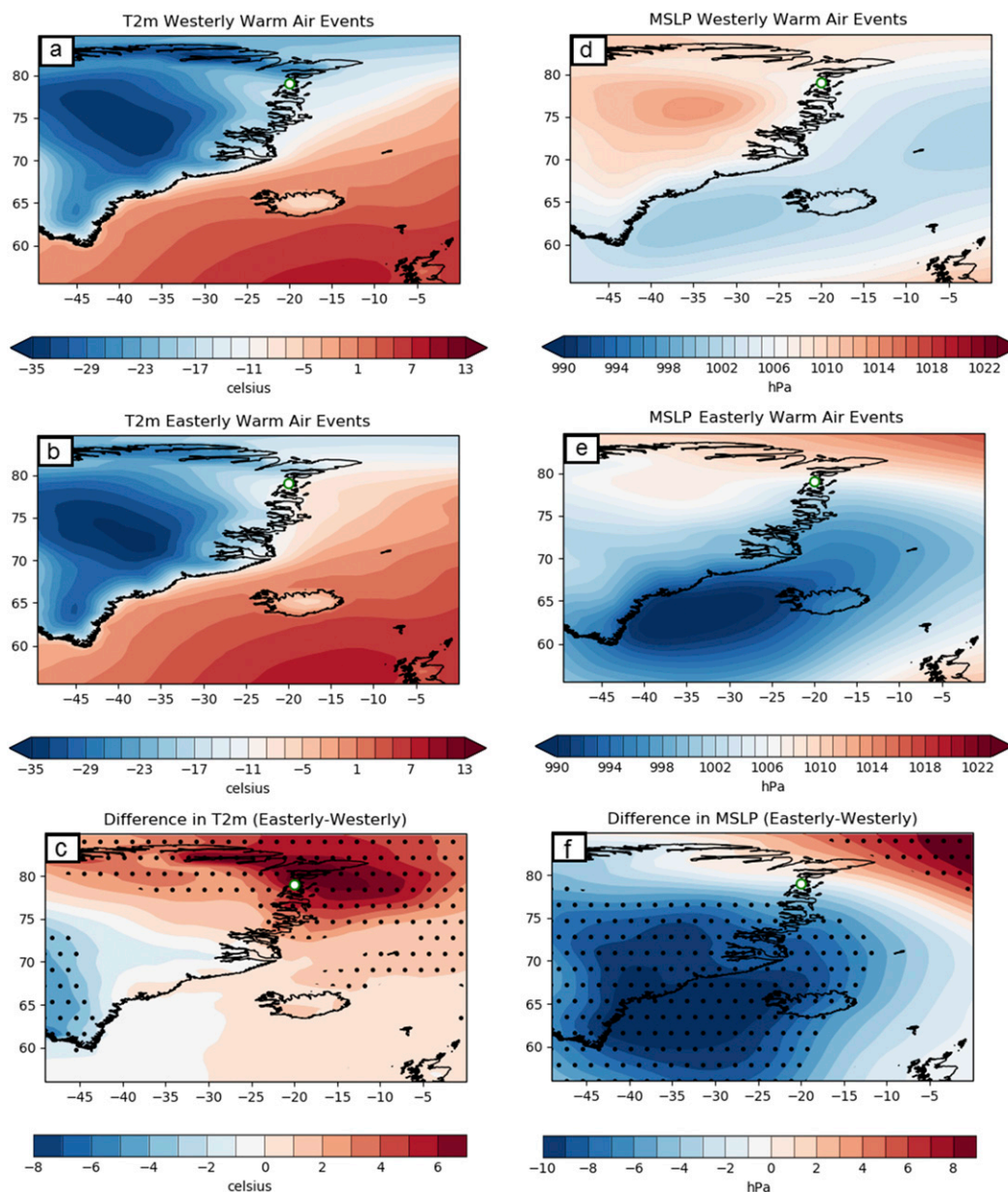
FIG. 7. Composite analysis of (a),(d) westerly and (b),(e) easterly warm-air events, and (c),(f) the difference between them (easterly − westerly), from ERA-I data, 1979–2017: (a)–(c) 2-m air temperature and (d)–(f) MSLP. 210 westerly events and 85 easterly events were used to create the composites. The dots infer that differences are statistically significant when using a *p* value of 0.01 for the FDR test by Wilks (2016).

publications within the Arctic have been limited to Svalbard (Rinke et al. 2017; Bednorz and Fortuniak 2011) and over the main pack of Arctic sea ice (Tjernström et al. 2015).

The highest number of warm-air events occurs in January (24% of events), and the fewest occur in March and November (approximately 15% in both) (Fig. 8). Figure 8 also shows that the fewest number of easterly events also occur in March (11 events), and the highest

number occur in December (25 events). The highest frequency of westerly warm-air events occurs in January (54 events) whereas March, November, and December all have a similarly low frequency (35–37 events). Warm-air events also occur within the last week of March, when average temperatures are starting to increase with the return of the polar day after the 20 February (for this location). This highlights the potential impact of the warm-air events on the mass balance of the glacier
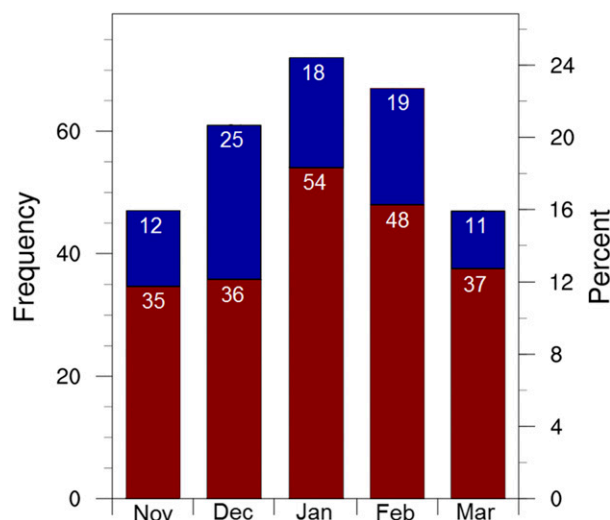
FIG. 8. A histogram displaying the frequency and percentage of easterly warm-air events (blue) and westerly warm-air events (red) from 1979 to 2017 from ERA-I. The number of warm-air events in each month is written on each bar.

surface. However, the average temperature change and daily temperature value associated with the warm-air events are not higher during March than in other months. The largest average temperature change is during December (13.2°C), and the smallest change is during March (12.0°C).

Similarly, there is no annual trend in the number of warm-air events, or in the maximum temperature change associated with events between 1979 and 2017. This suggests that the mechanisms responsible for warm-air events have not changed in frequency over the last 39 years. To further investigate the mechanisms responsible for the warm-air events, and to gain insight into the processes leading up to the temperature increase, a high-resolution atmospheric modeling case study is used. The warm-air event that has been simulated was from 30 November to 2 December 2014, as during this period, two rises in temperature were observed at KPC_U and KPC_L (Fig. 9b). Subsequently, a maximum hourly air temperature of −4.8°C was observed at KPC_U and −1.8°C at KPC_L, and a 48-h temperature increase of 18.7° and 17.6°C was observed at KPC_U and KPC_L, respectively (see the arrow on Fig. 3).

e. Warm-air advection case study

The WRF Model is an atmospheric numerical model and weather prediction tool used both operationally and for research purposes. The role of WRF in this study is to provide a deeper insight into the large wintertime air temperature variability identified from
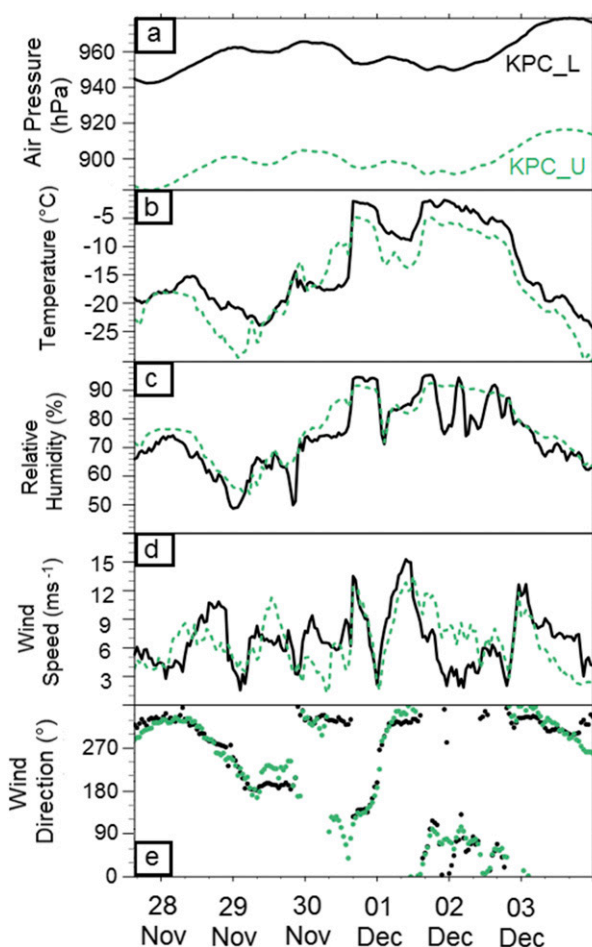

FIG. 9. The (a) hourly air pressure, (b) air temperature, (c) relative humidity, (d) wind speed, and (e) wind direction, from 28 Nov to 4 Dec 2014, observed at KPC_L and KPC_U stations. Main tick marks along the *x* axis are at 0000 UTC.

observations. For an overview of the model and information on the development and core of WRF, refer to Skamarock et al. (2008) and Powers et al. (2017). WRF has been tested for use in the polar regions (Bromwich et al. 2013; Hines and Bromwich 2017), and specifically for Greenland (Hines and Bromwich 2008). The release version of WRF, version 3.9.1.1, is used here. The physics options chosen for the case study here mirror those of the Hines and Bromwich (2008) study over Greenland. Because of the relatively complex topography and small-scale processes over 79N, high horizontal and vertical resolutions were required. Three one-way nested domains were used with horizontal resolutions of 25, 5, and 1 km (Fig. 1a). 70 levels in the vertical are used, with the first level at 12 m above surface and with 12 levels within the lowest 1 km. The MODIS land mask has been adjusted using the European Space Agency (ESA) Climate Change

Initiative (CCI) land-cover product, to allow for better representation of the floating glacier tongue (https://www.esa-landcover-cci.org/, last accessed 1 October 2018). Lateral and initial conditions in the outer domain, including sea ice cover and sea surface temperatures, are forced with ERA-I data (see section 3a for justification). The case study runs from 21 November to 10 December 2014, after a 24-h spinup period, in order to model the synoptic-scale evolution during that period. Because of the relatively short run time and the size of the domains, nudging was not used. This further allows us to assess the output from WRF, independent of the forcing data. Subsequent use of analysis nudging for the same setup in other tests has revealed a negligible difference between the runs with and without nudging.

During this particular event, the air temperature rose from a daily average of −24.5°C at KPC_U and −19.4°C at KPC_L on 28 November, to a daily average of −6.5° and −2.8°C on 2 December at KPC_U and KPC_L, respectively (Fig. 9b). This increase in temperatures was a result of two separate spikes in temperature. The first and largest increase in temperature occurred on the 30 November, when temperatures increased by 14.9°C in under five hours (Fig. 9b). The second, smaller temperature increase occurred between the 1 December and 2 December, when an increase of 7.0°C was observed over 9 h (Fig. 9b). Unfortunately, there are no in situ observations available on the floating ice shelf during this period. However, correlations are high (0.80 for temperature) and mean biases low (−1.7°C for temperature) between hourly observations taken at KPC_U and the WRF Model output for these locations. This gives confidence that the model is representing the near-surface conditions well and that values provided over the floating glacier surface can be assumed to be relatively accurate.

At 0000 UTC 29 November, a low pressure system developed to the southeast of Greenland (Fig. 10a). Prior to the onset of the temperature increase, there are weak westerly, katabatic winds present over the glacier (Fig. 10b), which generate localized mixing, resulting in slightly warmer (2°–4°C increase) temperatures at the near surface than farther aloft (Fig. 10c). The low pressure system deepens as it moves north between Iceland and the east coast of Greenland from 30 November to 2 December (Fig. 10d). Subsequently, relatively warm and moist air is advected onto the ice shelf of 79N on 30 November, leading to a sharp increase in air temperature (Figs. 9b and 10e). The wind strength then decreased for approximately 12 h overnight from 30 November to 1 December, allowing colder, continental air to flow down the glacier under katabatic

conditions that normally dominate the wind signal in this area (see the small temperature decrease in Fig. 9b). At approximately 1000 UTC 1 December, the easterly wind strength increases again, and warm air intruded back onto the floating glacier tongue, leading to maximum air temperatures of 0.2°C between 1800 UTC 1 December to 0000 UTC 2 December (Fig. 10d), and a skin temperature of 0°C was simulated for nine hours at the location of AWS 9602 and for 4 h at AWS 9604. For comparison, the average 1979–2017 December air temperature for this region is −27.2°C. The warmest part of the airmass lies below approximately 2-km height (Fig. 10f).

During the current case study, the warm-air mass is saturated up to approximately 2-km altitude, as simulated by the model and evident in Fig. 11. Furthermore, there is low-level cloud formation over 79N, as shown by the modeled vertical profiles of temperature and dewpoint temperature in Fig. 11 and the cloud-cover output in Fig. 12. Between 30 November and 2 December, WRF simulates near-persistent low-level clouds over 79N, at various altitudes between 100 m and 2 km (Fig. 12). Cloud-cover estimates from KPC_U and KPC_L confirm this with values between 0.95 and 1.0 from 30 November to 4 December (not shown), which provides more evidence for cloud formation during the warm-air advection episode. The vertical profiles of temperature and dewpoint temperature in Fig. 11 resemble those during similar warm-air advection events over the Arctic Ocean sea ice (Tjernström et al. 2019).

Table 4 highlights a number of the SEB components output from WRF during the case study. We adopt the convention that positive values of the turbulent fluxes and net radiation are toward the surface. As the ice surface was at the melting point for a number of hours during the warm-air event, a short discussion of the SEB components will follow to allow a first look into the changes of the individual components during these episodes. As the case study focuses on a period during winter, the net shortwave radiation is $0 \, \mathrm{W \, m^{-2}}$, and, consequently, the longwave components dominate the SEB. During hours when the skin temperature was at the melting point, the large incoming longwave radiation flux of $314.9 \, \mathrm{W \, m^{-2}}$ acts to balance out the large outgoing radiation from the ice surface ($315.6 \, \mathrm{W \, m^{-2}}$). Conversely, when excluding the period from 30 November to 2 December from the remaining case study period (to remove the influence of the warm-air event), there is a larger negative net longwave radiation ($-34.3 \, \mathrm{W \, m^{-2}}$) because of the smaller incoming longwave radiation compared to outgoing longwave radiation (Table 4). Therefore, the thick and low cloud cover is an important
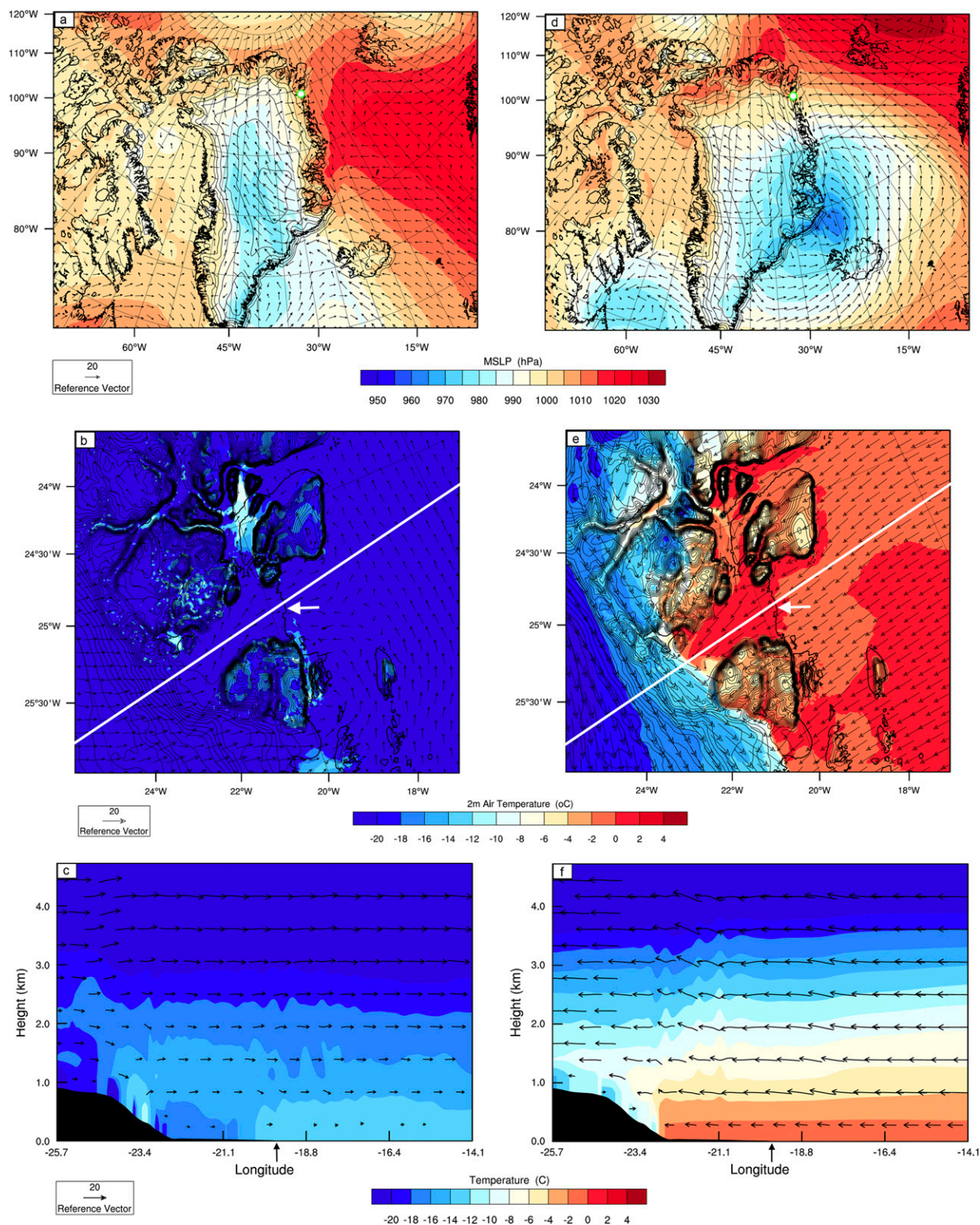
FIG. 10. (a) MSLP (colors) and 850 hPa winds (vectors) in the outer domain (D01), (b) 2-m temperature (colors) and 10-m winds (vectors) from the innermost domain (D03), and (c) vertical air temperature profile and vectors along a cross section of the floating tongue, at 0000 UTC 29 Nov 2014 from the WRF case study. (d)–(f) As in (a)–(c), but at 0000 UTC 2 Dec 2014. The white lines in (b) and (e) show the cross section used for (c) and (f). The white dot in (a) and (d) highlights the location of 79N. The white arrows in (b) and (e) and black arrows in (c) and (f) highlight the edge of the floating tongue. Black lines are the terrain contours from 0 to 1500 m in 200-m intervals. Panels (a)–(c) are conditions prior to the warm-air event, while (d)–(f) are during the warm-air event.
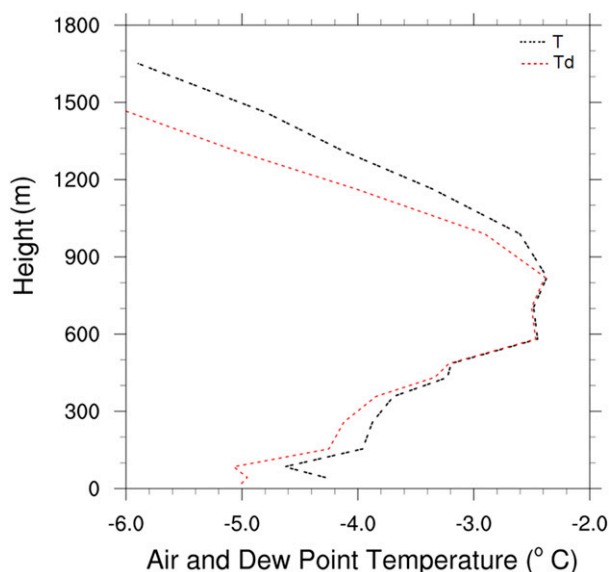
FIG. 11. Simulated vertical air temperature (black) and dewpoint temperature (red) at 0000 UTC 30 Nov 2014 at the 9604 AWS location. Low-level cloud presence between 600 m and 1 km is simulated by WRF.
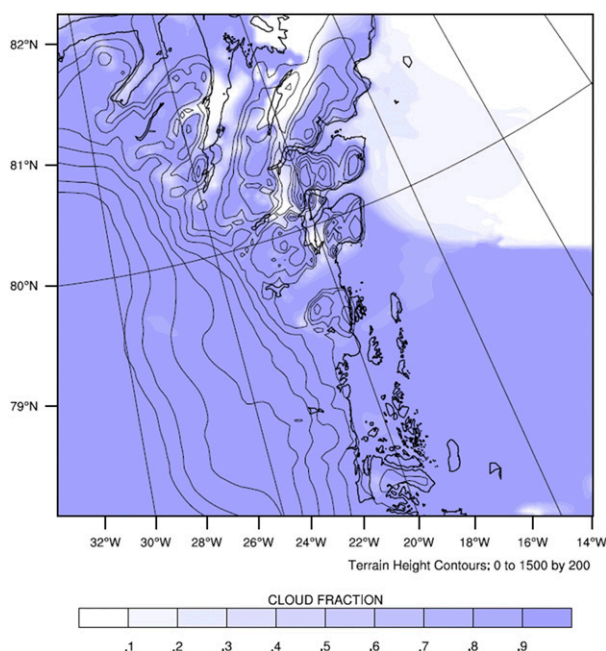

FIG. 12. The simulated cloud fraction from domain 2 of WRF at the sixth model level above the surface (approximately 400 m). Low-level clouds are substantial over the glacier and farther inland. Black lines are the terrain contours from 0 to 1500 m in 200-m intervals.

factor in controlling the SEB and melt potential during this warm-air event. The sensible heat flux (SH) became smaller during the warm-air event than during the remaining case study period. This is due to the smaller temperature gradient between the air and the ice surface during these warmer periods. The moist lower atmosphere during the warm-air event prevented sublimation of the surface ice during the whole case study, as evident in positive latent heat values, which increased during hours when the skin temperature was at the melting point (Table 4).

Because of the lack of SEB observations on the floating section of the glacier, we are unable to validate the results of the SEB components during the case study. The SEB components output from WRF have previously been validated for the Arctic in a number of studies (e.g., Hines et al. 2011; Aas et al. 2015; Porter et al. 2011). The largest bias between WRF and observations for the Arctic region are in the incoming shortwave radiation, for which WRF has a positive mean bias (Aas et al. 2015; Porter et al. 2011). Hines et al. (2011) also found that the largest biases in radiation components were during summer because of an overall warm temperature bias in WRF. Because of the lack of incoming shortwave radiation during the case study these particular biases are not present. The values of the SEB components simulated during this case study are of a similar magnitude to those observed by AWSs over the Antarctic during winter (van den Broeke et al. 2005). Our results are also similar

in magnitude and sign to those observed before and during a winter warm-air event that occurred north of Svalbard over the Arctic sea ice (Walden et al. 2017). Walden et al. (2017) observed an increase in the downwelling longwave radiation, a decrease in the sensible heat flux and only small changes in the latent heat flux, coinciding with the rise of air temperatures from $-40°$ to $-2.5°C$. These changes were largely attributed to an increase in cloud cover, as found in the current study.

There is little evidence for katabatic winds being responsible for the temperature jump event that occurred in November/December 2014, as shown by the lack of westerly winds on Fig. 10f. Furthermore, the observations from the KPC AWSs display an increase in relative humidity during the warm-air event (Fig. 9c), whereas a decrease or consistent low relative humidity would be expected with the presence of katabatic winds or foehn winds. Katabatic winds are present over the glacier prior to the temperature rise (Fig. 10b); however, they are weak over the floating tongue of the glacier, and lead to only small temperature increases through vertical mixing (Fig. 10c). Figure 13 illustrates the wind speed and direction every 6 h during the warm-air event from 30 November to 2 December (red dots). The wind during this period is from the east, and is not clustered within (north) westerly katabatic wind directions.

TABLE 4. Elements of the surface energy balance (SEB) during hours when the skin temperature (TSK) was equal to 0 during the case study (TSK = 0°C), and between 21–29 Nov and 3–9 Dec 2014 (TSK ≠ 0°C). All components are extracted from WRF at the grid point closest to AWS 9602. SW_{net} is the net shortwave radiation (incoming–outgoing), LW_{up} is outgoing longwave radiation, LW_{down} is incoming longwave radiation, SH is sensible heat flux, and LH is latent heat flux. All components have the units of $W\,m^{-2}$.

SEB component	TSK = 0°C	TSK ≠ 0°C
SW_{net}	0	0
LW_{up}	−315.6	−203.9
LW_{down}	314.9	169.6
SH	5.3	33.0
LH	4.9	0.7

Figure 13 also highlights the climatology of the wind direction over 79N. The largest cluster of wind directions are westerly to northwesterly (between approximately 250° and 360°), which displays the predominant katabatic winds. However, there are also regular periods when the wind direction is from the easterly sector, and a cluster of wind directions are located between 150° and 180°. Figure 13 also shows that the wind speeds during the case study event were strong (maximum 6-h average of 12.7 m s⁻¹), and fairly unusual for over the ice shelf. In the case study, there is evidently warm-air advection from the southeast on the floating tongue; however, at KPC_U, only 5% of warm-air events have a corresponding easterly (45°–135°) wind component. In comparison, approximately 30% of the warm-air events identified from ERA-I over the floating ice shelf (9604 location) have an easterly wind component. We hypothesize that only particularly strong episodes of easterly winds and associated warm-air advection are able to influence the conditions at the high altitudes (KPC stations), but more regularly they increase the air temperature over the floating ice shelf.

4. Conclusions

We investigate the near-surface meteorological conditions and climatology of the 79N glacier in order to widen our understanding of the processes in the region and provide a basis for further research into the processes responsible for glacier mass loss. In recent years, the ice has started thinning (Khan et al. 2014), and melt ponds are a persistent feature during summer. 79N is exposed to both a warming atmosphere and ocean, yet little is known about the atmospheric conditions in the 79N region. This study has identified a clear 3°C increase in air temperature over the last 39 years, in sync with, yet substantially exceeding the global trend of increasing temperatures. This trend has been observed in all regions of Greenland but is largest in the north.
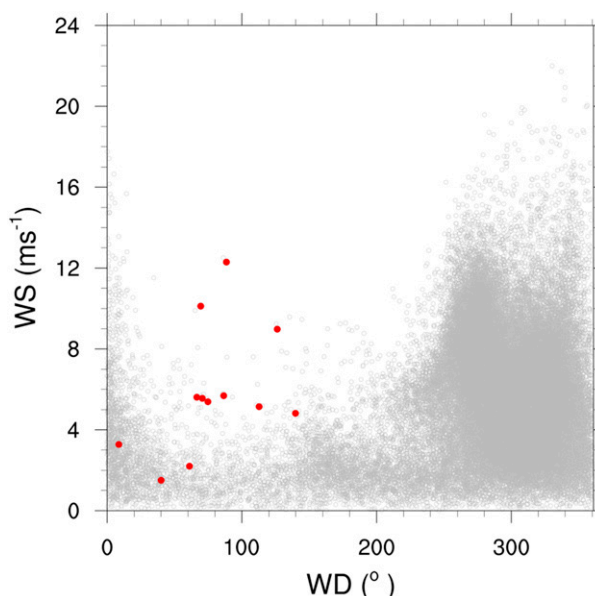

FIG. 13. The 6-hourly wind speed and direction from ERA-I at the 9602 location from 1979 to 2017 (gray hollow dots). Red dots indicate the 6-hourly (simulated) winds from the 9602 location, during the warm-air event (30 Nov–2 Dec).

The increased air temperature variability observed at the KPC AWSs during winter is consistent with increased cyclone activity during this time period and is evident through increased MSLP variability (Box et al. 2009). The wintertime air temperature variability over the whole GIS is 5 times greater than that in summer (Box et al. 2009). In summer, high pressure systems persist over Greenland that prohibit large interannual variability in air temperatures. As a consequence of high pressure over the continent, katabatic winds dominate the wind direction, as measured at all four AWS locations.

Despite the relatively short and intermittent observations on the floating glacier, they provide an insight into the average near-surface conditions, and provide evidence for high-amplitude but short-lived temperature increases from November to March. ERA-I data were used to expand the analysis of the near-surface conditions. The average annual temperature over 79N glacier is −16.7°C, which increases to an average of −0.4°C during summer. The warm-air events were resolved by ERA-I and are present every year.

Over 79N, two mechanisms appear to be responsible for the warm-air events; warm-air advection and mixing from katabatic winds. In a study of a similar process occurring over Svalbard, warm-air advection accounted for 95% of the winter warming signal (Bednorz and Fortuniak 2012). However, katabatic winds have been observed to increase the near-surface temperatures

over ice (e.g., Parish and Bromwich 1989; Vihma et al. 2011). The case study presented here provides evidence for warm-air advection as a mechanism responsible for a number of the events, however, it is clear that mixing from katabatic winds is also a mechanism responsible for warm-air events in the 79N region.

The local climate signal in the northeast of Greenland was highlighted by Abermann et al. (2017), who found that the latitudinal pattern of temperatures (decreasing temperature with increasing northerly latitude) was not observed in the northeast because of deviations from the norm for temperature and pressure. As monthly average temperature conditions were assessed as part of the Abermann et al. (2017) study, we are unable to see whether warm-air events are responsible for these departures; however, only the stations in the northeast of Greenland displayed the increases in temperature. The two AWSs used in the northeast of Greenland by Abermann et al. (2017) were over 187 km away from 79N (80.65° and 81.60°N), but also display clear deviations from the conditions expected at this latitude. Therefore, we suggest that warm-air events may reach farther north than just 79N glacier, which may indicate a synoptic-scale influence (such as warm-air advection) over local-scale influence (katabatic winds). Although both warm-air advection and katabatic winds are observed in other coastal polar regions, the analysis here cannot be broadened to that of all regions experiencing coreless winters because of the differing synoptic and local conditions.

During the simulated event in November–December 2014, near-surface temperatures on the 79N ice shelf were above freezing; 27°C above normal seasonal temperatures. The warm-air events not only have an impact on the near-surface atmosphere, but also on the ice surface, as skin temperatures were simulated to have risen to the melting point. During the case study presented, the ice surface was at the melting point for up to 9 h, while simultaneously, moist conditions lead to cloud formation. The cloud formation subsequently caused an increase in the incoming longwave radiation, which was the largest contributing factor to the positive net radiation and warming surface.

For polar glaciers, surface mass loss is often restricted to the summer season; however, a recent study by (Kuipers Munneke et al. 2018) shed light on the impact of winter melting episodes over the Antarctic Peninsula. Over 79N, over 15% of the warm-air events occur during March, when the air temperatures are rising with the increasing solar radiation. Therefore, ice melt may be initiated, if only for a short period, during the warm-air events. While detailed analyses of SEB patterns and their driving atmospheric influences over

79N and the northeast ice stream are planned for future work, this study presents a first glance at the potential links between the warm-air events and surface melting. Because of the multiple processes at play, the influence of the warm-air events on the surface energy and mass balances is complicated, yet, because of the persistence of the warm-air events, this impact must be further addressed in future work. Now that the current meteorological and climatological conditions have been established, we are a step closer to understanding the atmosphere-glacier relationship over 79N under current and future conditions.

REFERENCES

Aas, K. S., and Coauthors, 2015: A comparison between simulated and observed surface energy balance at the Svalbard Archipelago. *J. Appl. Meteor. Climatol.*, **54**, 1102–1119, https://doi.org/10.1175/JAMC-D-14-0080.1.

Abermann, J., B. Hansen, M. Lund, S. Wacker, M. Karami, and J. Cappelen, 2017: Hotspots and key periods of Greenland climate change during the past six decades. *Ambio*, **46**, 3–11, https://doi.org/10.1007/s13280-016-0861-y.

Bednorz, E., and K. Fortuniak, 2011: The occurrence of coreless winters in central Spitsbergen and their synoptic conditions. *Polar Res.*, **30**, 12218, https://doi.org/10.3402/polar.v30i0.12218.

——, and ——, 2012: Coreless winters in the European sector of the Arctic and their synoptic conditions. *Pol. Polar Res.*, **33**, 19–34, https://doi.org/10.2478/v10183-012-0007-2.

Box, J. E., L. Yang, D. H. Bromwich, and L.-S. Bai, 2009: Greenland ice sheet surface air temperature variability: 1840–2007. *J. Climate*, **22**, 4029–4049, https://doi.org/10.1175/2009JCLI2816.1.

Bromwich, D. H., F. O. Otieno, K. M. Hines, K. W. Manning, and E. Shilo, 2013: Comprehensive evaluation of Polar Weather Research and Forecasting Model performance in the Antarctic. *J. Geophys. Res. Atmos.*, **118**, 274–292, http://doi.wiley.com/10.1029/2012JD018139.

Carr, J. R., C. R. Stokes, and A. Vieli, 2013: Recent progress in understanding marine-terminating Arctic outlet glacier response

to climatic and oceanic forcing. *Prog. Phys. Geogr.*, **37**, 436–467, https://doi.org/10.1177/0309133313483163.

Dee, D. P., and Coauthors, 2011: The ERA-Interim reanalysis: Configuration and performance of the data assimilation system. *Quart. J. Roy. Meteor. Soc.*, **137**, 553–597, https://doi.org/10.1002/qj.828.

Gelaro, R., and Coauthors, 2017: The Modern-Era Retrospective Analysis for Research and Applications, version 2 (MERRA-2). *J. Climate*, **30**, 5419–5454, https://doi.org/10.1175/JCLI-D-16-0758.1.

Graham, R. M., and Coauthors, 2017: A comparison of the two Arctic atmospheric winter states observed during N-ICE2015 and SHEBA. *J. Geophys. Res. Atmos.*, **122**, 5716–5737, http://doi.wiley.com/10.1002/2016JD025475.

Hall, D. K., R. S. Williams, S. B. Luthcke, and N. E. Digirolamo, 2008: Greenland ice sheet surface temperature, melt and mass loss: 2000–06. *J. Glaciol.*, **54** (184), 81–93, https://doi.org/10.3189/002214308784409170.

Heinemann, G., and T. Klein, 2002: Modelling and observations of the katabatic flow dynamics over Greenland. *Tellus*, **54A**, 542–554, https://doi.org/10.1034/j.1600-0870.2002.201401.x.

Hines, K. M., and D. H. Bromwich, 2008: Development and testing of Polar Weather Research and Forecasting (WRF) Model. Part I: Greenland ice sheet meteorology. *Mon. Wea. Rev.*, **136**, 1971–1989, https://doi.org/10.1175/2007MWR2112.1.

——, and ——, 2017: Simulation of late summer Arctic clouds during ASCOS with Polar WRF. *Mon. Wea. Rev.*, **145**, 521–541, https://doi.org/10.1175/MWR-D-16-0079.1.

——, ——, L. Bai, M. Barlage, and A. G. Slater, 2011: Development and testing of Polar WRF. Part III: Arctic land. *J. Climate*, **24**, 26–48, https://doi.org/10.1175/2010JCLI3460.1.

Huybrechts, P., C. Mayer, H. Oerter, and F. Jung-Rothenhäusler, 1999: Climate change and sea level: Ice-dynamics and mass-balance studies on the Greenland ice sheet. EPIC3 Rep. on the Contribution of the Alfred Wegener Institute to EU Contract ENV4-CT95-0124, European Commission, DG XII, 18 pp., https://epic.awi.de/id/eprint/3663/1/Huy1999b.pdf.

Joughin, I., W. Abdalati, and M. Fahnestock, 2004: Large fluctuations in speed on Greenland's Jakobshavn Isbrae glacier. *Nature*, **432**, 608–610, https://doi.org/10.1038/nature03130.

Khan, S. A., and Coauthors, 2014: Sustained mass loss of the northeast Greenland ice sheet triggered by regional warming. *Nat. Climate Change*, **4**, 292–299, https://doi.org/10.1038/nclimate2161.

Kuipers Munneke, P., and Coauthors, 2018: Intense winter surface melt on an Antarctic ice shelf. *Geophys. Res. Lett.*, **45**, 7615–7623, http://doi.wiley.com/10.1029/2018GL077899.

Larsen, N. K., L. B. Levy, A. E. Carlson, C. Buizert, J. Olsen, A. Strunk, A. A. Bjørk, and D. S. Skov, 2018: Instability of the Northeast Greenland Ice Stream over the last 45,000 years. *Nat. Commun.*, **9**, 1872, https://doi.org/10.1038/s41467-018-04312-7.

Leeson, A. A., E. Eastoe, and X. Fettweis, 2018: Extreme temperature events on Greenland in observations and the MAR regional climate model. *Cryosphere*, **12**, 1091–1102, https://doi.org/10.5194/tc-12-1091-2018.

Mayer, C., N. Reeh, F. Jung-Rothenhäusler, P. Huybrechts, and H. Oerter, 2000: The subglacial cavity and implied dynamics under Nioghalvfjerdsfjorden Glacier, NE-Greenland. *Geophys. Res. Lett.*, **27**, 2289–2292, https://doi.org/10.1029/2000GL011514.

——, and Coauthors, 2018: Large ice loss variability at Nioghalvfjerdsfjorden Glacier, Northeast-Greenland. *Nat. Commun.*, **9**, 2768, https://doi.org/10.1038/s41467-018-05180-x.

Mernild, S. H., E. Hanna, J. C. Yde, J. Cappelen, and J. K. Malmros, 2014: Coastal Greenland air temperature extremes and trends 1890–2010: Annual and monthly analysis. *Int. J. Climatol.*, **34**, 1472–1487, https://doi.org/10.1002/joc.3777.

Mölg, T., N. J. Cullen, D. R. Hardy, M. Winkler, and G. Kaser, 2009: Quantifying climate change in the tropical midtroposphere over East Africa from glacier shrinkage on Kilimanjaro. *J. Climate*, **22**, 4162–4181, https://doi.org/10.1175/2009JCLI2954.1.

Orsi, A. J., and Coauthors, 2017: The recent warming trend in North Greenland. *Geophys. Res. Lett.*, **44**, 6235–6243, https://doi.org/10.1002/2016GL072212.

Parish, T. R., and D. H. Bromwich, 1989: Instrumented aircraft observations of the katabatic wind regime near Terra Nova Bay. *Mon. Wea. Rev.*, **117**, 1570–1585, https://doi.org/10.1175/1520-0493(1989)117<1570:IAOOTK>2.0.CO;2.

Porter, D. F., J. J. Cassano, and M. C. Serreze, 2011: Analysis of the Arctic atmospheric energy budget in WRF: A comparison with reanalyses and satellite observations. *J. Geophys. Res.*, **116**, D22108, http://doi.wiley.com/10.1029/2011JD016622.

Powers, J. G., and Coauthors, 2017: The Weather Research and Forecasting Model: Overview, system efforts, and future directions. *Bull. Amer. Meteor. Soc.*, **98**, 1717–1737, https://doi.org/10.1175/BAMS-D-15-00308.1.

Reeh, N., C. Mayer, H. Miller, H. H. Thomsen, and A. Weidick, 1999: Present and past climate control on fjord glaciations in Greenland: Implications for IRD-deposition in the sea. *Geophys. Res. Lett.*, **26**, 1039–1042, https://doi.org/10.1029/1999GL900065.

Reeves-Eyre, J. E. J., and X. Zeng, 2017: Evaluation of Greenland near surface air temperature datasets. *Cryosphere*, **11**, 1591–1605, https://doi.org/10.5194/tc-11-1591-2017.

Rinke, A., M. Maturilli, R. M. Graham, H. Matthes, D. Handorf, L. Cohen, S. R. Hudson, and J. C. Moore, 2017: Extreme cyclone events in the Arctic: Wintertime variability and trends. *Environ. Res. Lett.*, **12**, 094006, https://doi.org/10.1088/1748-9326/aa7def.

Schaffer, J., W.-J. von Appen, P. A. Dodd, C. Hofstede, C. Mayer, L. de Steur, and T. Kanzow, 2017: Warm water pathways toward Nioghalvfjerdsfjorden Glacier, Northeast Greenland. *J. Geophys. Res. Oceans*, **122**, 4004–4020, https://doi.org/10.1002/2016JC012462.

Seroussi, H., M. Morlighem, E. Rignot, E. Larour, D. Aubry, H. Ben Dhia, and S. S. Kristensen, 2011: Ice flux divergence anomalies on 79north Glacier, Greenland. *Geophys. Res. Lett.*, **38**, L09501, http://doi.wiley.com/10.1029/2011GL047338.

Shepherd, A., and Coauthors, 2012: A reconciled estimate of ice-sheet mass balance. *Science*, **338**, 1183–1189, https://doi.org/10.1126/science.1228102.

Skamarock, W. C., and Coauthors, 2008: A description of the Advanced Research WRF version 3. NCAR Tech. Note NCAR/TN-475+STR, 113 pp., https://doi.org/10.5065/D68S4MVH.

Sotiropoulou, G., M. Tjernström, J. Savre, A. M. L. Ekman, K. Hartung, and J. Sedlar, 2018: Large-eddy simulation of a warm-air advection episode in the summer Arctic. *Quart. J. Roy. Meteor. Soc.*, **144**, 2449–2462, http://doi.wiley.com/10.1002/qj.3316.

Suparta, W., F. N. A. Bakar, and M. Abdullah, 2012: Coreless winter characteristics observed with global positioning system receivers over Antarctic and Arctic regions. *Amer. J. Appl. Sci.*, **9**, 1203–1213, https://doi.org/10.3844/ajassp.2012.1203.1213.

Thomsen, H. H., N. Reeh, O. Olesen, C. E. Boggild, W. Starzer, A. Weidick, and A. K. Higgins, 1997: The Nioghalvfjerdsfjorden glacier project, North-East Greenland: A study of ice sheet response to climatic change. *Geol. Greenl. Surv. Bull.*, **176**, 95–103.

Tjernström, M., and Coauthors, 2015: Warm-air advection, air mass transformation and fog causes rapid ice melt. *Geophys. Res. Lett.*, **42**, 5594–5602, https://doi.org/10.1002/2015GL064373.

——, M. Shupe, I. Brooks, P. Achtert, J. Prytherch, and J. Sedlar, 2019: Arctic summer air-mass transformation, surface inversions and the surface energy budget. *J. Climate*, **32**, 769–789, https://doi.org/10.1175/JCLI-D-18-0216.1.

van As, D., 2011: Warming, glacier melt and surface energy budget from weather station observations in the Melville Bay region of northwest Greenland. *J. Glaciol.*, **57**, 208–220, https://doi.org/10.3189/002214311796405898.

——, and R. Fausto, 2011: Programme for Monitoring of the Greenland Ice Sheet (PROMICE): First temperature and ablation records. *Geol. Surv. Denmark Greenl. Bull.*, **23**, 73–76.

——, and Coauthors, 2014: Katabatic winds and piteraq storms: Observations from the Greenland ice sheet. *Geol. Surv. Denmark Greenl. Bull.*, **31**, 83–86.

——, and Coauthors, 2018: Reconstructing Greenland Ice Sheet meltwater discharge through the Watson River (1949–2017). *Arct. Antarct. Alp. Res.*, **50**, S100010, https://doi.org/10.1080/15230430.2018.1433799.

van den Broeke, M., D. van As, C. Reijmer, and R. van de Wal, 2004: Assessing and improving the quality of unattended radiation observations in Antarctica. *J. Atmos. Oceanic Technol.*, **21**, 1417–1431, https://doi.org/10.1175/1520-0426(2004)021<1417:AAITQO>2.0.CO;2.

——, C. Reijmer, D. Van As, R. Van de Wal, and J. Oerlemans, 2005: Seasonal cycles of Antarctic surface energy balance from automatic weather stations. *Ann. Glaciol.*, **41**, 131–139, https://doi.org/10.3189/172756405781813168.

Vihma, T., E. Tuovinen, and H. Savijärvi, 2011: Interaction of katabatic winds and near-surface temperatures in the Antarctic. *J. Geophys. Res.*, **116**, D21119, https://doi.org/10.1029/2010JD014917.

Walden, P., S. R. Hudson, L. Cohen, S. Y. Murphy, and M. A. Granskog, 2017: Atmospheric components of the surface energy budget over young sea ice: Results from the N-ICE2015 campaign. *J. Geophys. Res. Atmos.*, **122**, 8427–8446, https://doi.org/10.1002/2016JD026091.

Wexler, H., 1958: The "kernlose" winter in Antarctica. *Geophys. Meteor.*, **6**, 577–595.

Wilks, D. S., 2016: "The stippling shows statistically significant grid points": How research results are routinely overstated and overinterpreted, and what to do about it. *Bull. Amer. Meteor. Soc.*, **97**, 2263–2273, https://doi.org/10.1175/BAMS-D-15-00267.1.